Dynamics of longitudinal Hawaiian hotspot motion and the formation of the Hawaiian-Emperor Bend

Jiashun Hu
hujs@sustech.edu.cn

Southern University of Science and Technology https://orcid.org/0000-0003-1007-6837

Jie Zhang
Southern University of Science and Technology

Physical Sciences - Article

Keywords:

Posted Date: March 27th, 2024

DOI: https://doi.org/10.21203/rs.3.rs-4168500/v1

Additional Declarations: There is **NO** Competing Interest.

Dynamics of longitudinal Hawaiian hotspot motion and the formation of the Hawaiian-Emperor Bend

Jie Zhang[1], Jiashun Hu[1,*]

[1]*Department of Earth and Space Sciences, Southern University of Science and Technology, Shenzhen, China, 518055*

**Email: hujs@sustech.edu.cn*

Abstract

Formation of the Hawaiian-Emperor Bend has been a key geological puzzle that involves both plate tectonics and plume dynamics. Constrained by paleomagnetic data, southward hotspot motion has been considered a major contributor to the formation of the bend, but the role of longitudinal hotspot motion remains largely overlooked. Here, using geometric analysis with constraints from plate kinematics, we show a significant longitudinal hotspot motion is required to fit the Hawaiian-Emperor Chain. Further application of global mantle convection models reveals a westward (by ~6°) and then an eastward (by ~2°) hotspot drift in addition to the southward motion before and after the bend, with the westward motion primarily controlled by the intraoceanic subduction in Northeast Pacific. While both the westward and southward motion are required to fit the seamount chain, the former contributes ~20 degrees to the bend angle, larger than the later, challenging traditional views. Combining geodynamically-predicted Pacific Plate motion change at 47 Ma, our model provides a nearly perfect fit to the seamount chain, suggesting plate-mantle reorientation as the ultimate cause. It also suggests that the Hawaiian plume conduit is tilted towards the southwest, solving the long-lasting debate on the source of the Hawaiian plume among seismological studies.

The Hawaiian-Emperor Chain in the Northwestern Pacific Ocean features a conspicuous 60° bend that has been the subject of multiple interpretations, including an abrupt change in Pacific plate motion in the Eocene (~47 Ma)[1–3], a rapid southward drift of the Hawaiian hotspot before the bend[4–10], or a combination of the two factors[11,12]. Different plate reconstructions have suggested various degrees of Pacific Plate motion change at 47 Ma, but none of them can solely account for the formation of the Hawaiian-Emperor Bend (HEB)[3]. The latest geodynamic model has predicted a maximum of 30-35° in Pacific Plate motion change, on the condition that the Kronotsky subduction in North Pacific had existed[11], implying that the southward motion of the Hawaiian hotspot is required to account for the HEB. This is consistent with palaeomagnetic data that suggest a rapid 11°-15° southward motion of the hotspot between 81 Ma and 0 Ma[4,6,9]. However, the exact hotspot trajectory still remains disputed, leading to the long debate on the relative contribution of Pacific Plate motion change and hotspot drift to the formation of the HEB.

In contrast to most geodynamic models that demonstrate a prevailing southward or southeastward motion of the Hawaiian hotspot[5,7], geometric simulation and inference of plate reconstructions[5,3,11] find a large westward component in the motion of the Hawaiian hotspot before 47Ma (Fig. 1). Assuming a 30-35° Pacific Plate motion change following the geodynamic prediction by Hu et al. (2022)[11], which is largely consistent with the recent plate reconstruction by Müller et al. (2019)[13], the derived hotspot motion shows a westward component of ~5° before 47 Ma (Fig. 1a). This westward motion needs to be much larger, reaching more than 15°, if the Pacific Plate motion remains unaltered before and after the bend (Fig. 1a, b). However, there is no geodynamic justification for a significant westward component in the drift of the hotspot. The solution to this discrepancy arguably represents one of the major remaining pieces of the puzzle to the formation of HEB, given that other important factors including Pacific Plate motion change and southward hotspot drift have more or less been constrained by observations with their underlying mechanisms explored by geodynamic modeling. In the following sections, we aim to investigate the longitudinal motion of the Hawaiian hotspot using paleogeographically constrained global mantle convection models since the early Mesozoic, and further constrain its contribution to the formation of the HEB. We find changes in longitudinal motion of hotspot can contribute significantly to the HEB, complementing earlier studies that focus mostly on the southward migration of the hotspot or the change in Pacific Plate motion.

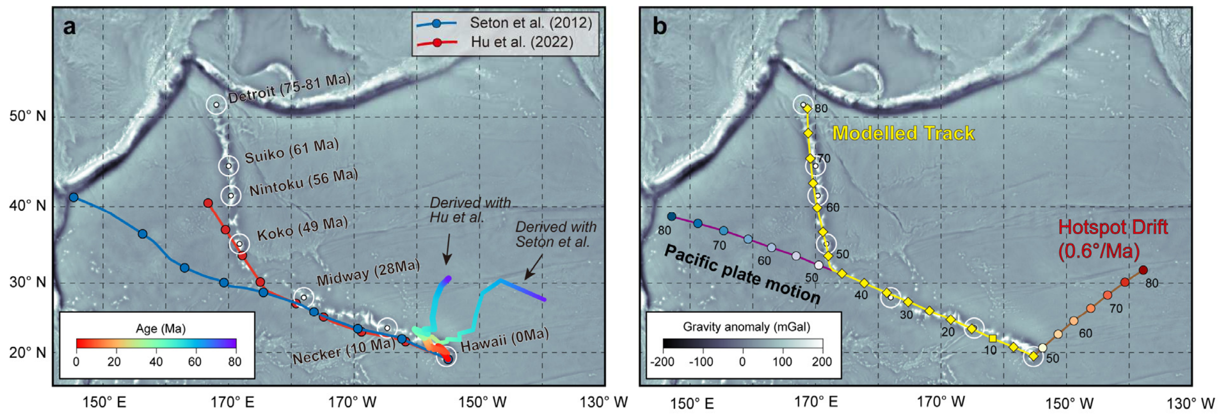

Fig.1. Geometric simulation of the Hawaiian hotspot motion. a, Inferred Hawaiian hotspot trajectory assuming the Pacific Plate motion predicted by the geodynamic model of Hu et al. (2022)[11] and inferred hotspot trajectory using the absolute kinematic model of Seton et al. (2012)[14]. **b**, Inferred hotspot motion (modified from Torsvik et al. (2017)[3]) that assumes the Pacific plate moves with a constant angular velocity to the north-west (ω=0.72°/Ma, Euler pole: 68°S, 103°E). This requires south-westward hotspot motion (by 20.1°about the Euler pole at 44.3°S, 274.6°E, ~0.6°/Ma) in order to form the Emperor Seamounts during the 80-47 Ma period and reproduce the geometry of the Hawaiian-Emperor Chain. The background shows gravity anomaly.

Predicted hotspot drift based on conventional plate reconstructions

Engebretson et al. (1985)[15] developed a quantitative plate model that covers the past 180 million years and divided the ancient Panthalassa Ocean into five distinct plates: Pacific, Izanagi, Farallon, Phoenix, and Kula. They proposed that the Farallon plate continuously underwent "Andean-type" subduction beneath the entire length of the North American continental margin, while also explicitly acknowledging that this interpretation was influenced by geological evidence from land. Despite this caveat, the idea of Farallon-beneath-continent subduction has been widely adopted in modern reconstructions of the region (Fig. 2a, c). We first test three plate reconstructions to predict the Hawaiian hotspot drift, with two plate reconstructions adopting the conventional idea of Panthalassa Ocean evolution and “Andean-type” subduction beneath North America including Müller et al. (2016) (“M16”)[16] and Müller et al. (2019) (“M19”)[13], and one additional plate reconstruction that further incorporates the Kronotsky intraoceanic subduction in North Pacific based on Hu et al. (2022) (“Hu22”)[11]. We export the kinematics and thermal ages of plates from these plate reconstructions at every one million years and integrate them into global mantle convection models[17] (Extended Data Fig. 1). Subduction of slabs from 250/230 Ma disturbs the basal thermochemical layer, which further generates mantle plumes whose surface trajectories are recorded and compared between different models. Please see Methods for more detailed model description.

For all the three models, two thermochemical piles have gradually developed beneath the Africa and Pacific Ocean, resembling the seismologically observed Large Low Velocity Provinces (LLVPs) (Extended Data Fig. 2). Multiple dynamic plumes have emerged primarily in the vicinity of these LLVPs. Among them, the Hawaiian plume erupted around 120 Ma at a latitude higher than present day (Extended Data Fig. 3a, c). After its inception, the Hawaiian hotspot moved steadily southward and eventually ends up on the eastern side of the Hawaiian Islands for M16 and Hu22 and southern side for M19. The drift path of the Hawaiian hotspot in Hu22 is very similar to that in M16, indicating that the Kronotsky intraoceanic subduction system had a minor impact on the southward motion of the Hawaiian plume.

Subsequently, we widely explore the viscosity and density parameters of slabs and thermochemical layer in the models M16 and Hu22, new models named "M16_Adj" and "Hu22_Adj", and find a set of parameters that can better fit the present-day location of the Hawaiian hotspot (M16_Adj, Hu22_Adj in Extended Data Table 2; Extended Data Fig. 3d, e). Despite the wide range of parameters explored with some of them even falling outside the proper range, the prevailing southward motion of the hotspot remains largely the same. For all the five models, no substantial westward motion in the trajectories of the Hawaiian hotspot is observed, similar to the prediction by Hassan et al. (2016)[7] (Extended Data Fig. 3f). The predominant southward motion of the Hawaiian hotspot is dominated by the prevailing southward lower mantle flow (Extended Data Fig. 4). The southeastward mantle flow induced by the Izanagi slab in the Northwest Pacific and the southwestward mantle flow caused by the Farallon slab in the Northeast Pacific converge in the central Pacific, resulting in a strong net southward mantle flow that drives the continued southward migration of the Hawaiian plume[7].

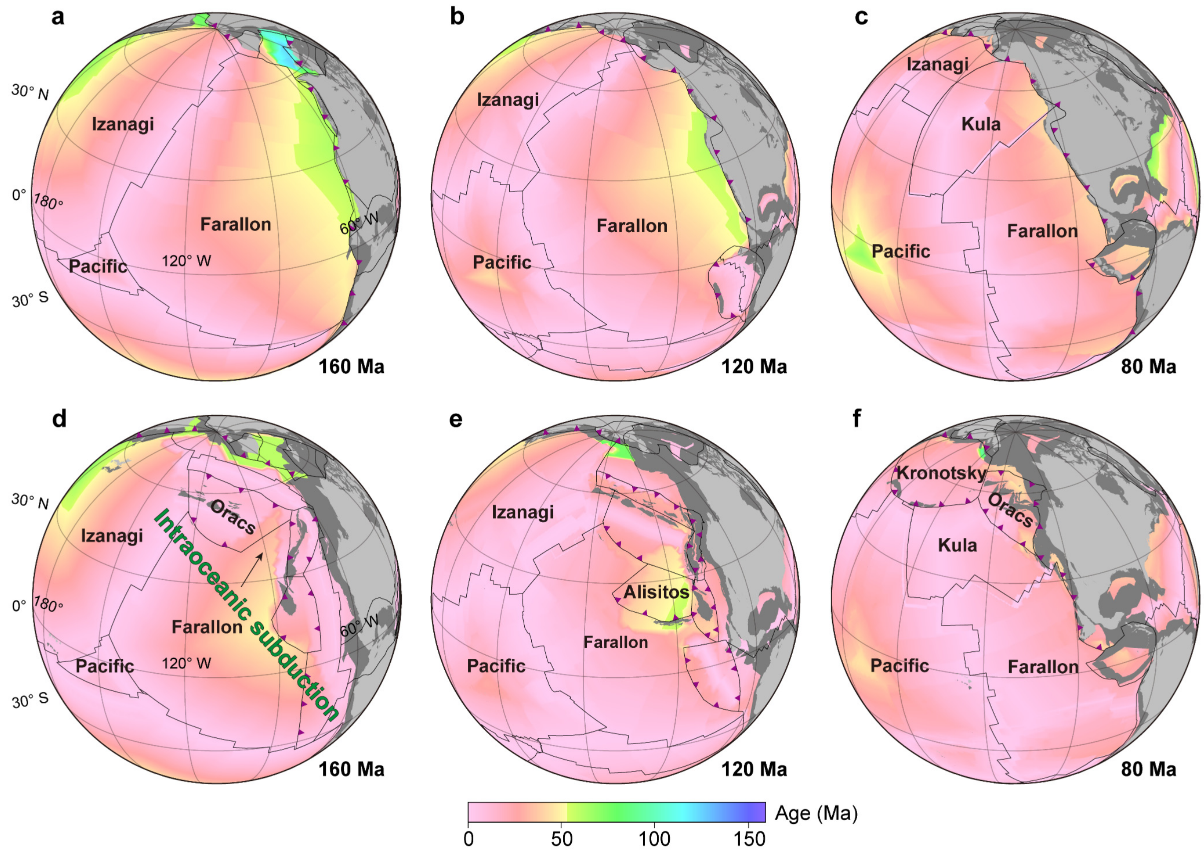

Fig.2. Alternative plate reconstruction models from Early Jurassic to Late Cretaceous. a-c, The traditional plate reconstruction of Müller et al. (2019)[13] that assumes "Andean-type" subduction beneath North America. **d-f**, The plate reconstruction of Clennett et al. (2020)[18] that considers the intraoceanic subduction system in the northeastern Pacific and is further modified to incorporate a revised Kronotsky intraoceanic subduction proposed by Hu et al. (2022)[11] in the northern Pacific. Background colour indicates the seafloor age.

Northeastern Pacific intra-oceanic subduction and southwestward hotspot drift

We tentatively test another plate reconstruction that incorporates the intraoceanic subduction system in northeastern Pacific (Extended Data Fig. 2d, f). The conventional "Andean-type" subduction beneath North America has been challenged on geological grounds and more recently by tomographic images. Jurassic-Cretaceous arc assemblages, accretionary complexes, and ophiolites comprise large tracts of the North American Cordillera[19,20]. The differing histories of these terranes, as revealed by lithological, paleomagnetic, and fossil fauna data, suggest intra-oceanic subduction west of North America, similar to the present-day southwest Pacific[21–26]. Such a plate configuration is consistent with "tomotectonic analysis" that uses tomographic images as main constraints[27,28]. Recently, Clennett et al. (2020)[18] had presented the first plate model with continuously closing boundaries of the Late Jurassic-Cretaceous eastern Pacific intra-oceanic arc system, from 170 Ma to 0 Ma (Fig. 2d-f; Extended Data Fig. 5a, c). Compared to previous reconstruction models, these intraoceanic subductions brought the Farallon subduction closer to the west, providing a possible dynamical explanation for the westward drift of the Hawaiian hotspot (Fig. 2).

To keep it consistent with our previous study[11], we make some modifications to the Kronotsky Plate of the Clennett et al. (2020)[18] reconstruction model (Extended Data Fig. 5d-f), and then restart the model M19 from 170 Ma using the same rheological parameters, but with the imposed surface kinematics and seafloor ages consistent with this revised reconstruction. This model represents our reference model (Model 1 in Extended Data Table 2). In this model, the Hawaiian plume was generated at ~120 Ma and the hotspot has drifted southward by approximately 11-12° over the past 85 Ma (Fig. 3; Fig. 4a, c). The majority of this movement occurred before the formation of the bend (85-47 Ma), during which the hotspot drifted southward by 7-8° at a velocity of approximately 36 mm/yr. The remaining 3-4° of southward drift occurred after the bend at a velocity of around 15 mm/yr (Fig. 4a, c). This southward migration process is consistent with palaeomagnetic data and latitudinal estimates of surface motions of the Hawaiian hotspot (Fig. 4a, c) [4,29].

An important finding of our reference model is the westward drift of the Hawaiian hotspot. Specifically, between 85-47 Ma, the Hawaiian hotspot underwent a rapid westward drift, shifting a total of ~6° during this period, while simultaneously moving southward. After 45 Ma, the time of the HEB, the westward drift stopped and the direction of the hotspot motion changed from northeast-southwest to northwest-southeast. The hotspot then drifted eastward by about 2-3° to its present longitude (Fig. 3; Fig. 4a, b). We find this pattern is a robust feature. Using distinct model parameters, including the buoyancy ratios of the basal thermochemical layer and the eclogitized oceanic crust, the activation energy of slabs and the background mantle viscosity profile (Extended Data Table 2), all models show similar patterns in the longitudinal motion (Extended Data Fig. 6), except model 7 that has too strong slabs that pushed the Hawaiian plume continuously toward the west. While some models show a slowdown of westward motion at ~45 Ma first and then a shift to eastward motion, others exhibit a more abrupt shift from westward to eastward motion at ~45 Ma (e.g. Extended Data Fig. 6g, h, j). This reflects different amount of time needed to readjust the plume conduit. The modeled velocity field showed that when the northeastern Pacific intraoceanic subduction existed, there would be a strong southwestward mantle flow in the lower mantle beneath the northeast Pacific between 80 Ma and 50 Ma, while this southwestward flow field diminished at ~40 Ma, corresponding to the end of the southwestward drift of the Hawaiian hotspot (Fig. 3; Extended Data Fig. 7). We suggest that this strong southwestward flow field was caused by the lower-mantle slab from the intraoceanic subduction in the northeastern Pacific. In the five comparison models, we do not find such strong southwestward mantle flow due to the absence of this intraoceanic subduction (Extended Data Fig. 4), and thus there is only a rapid southward motion of the Hawaiian plume (Extended Data Fig. 3a-e).

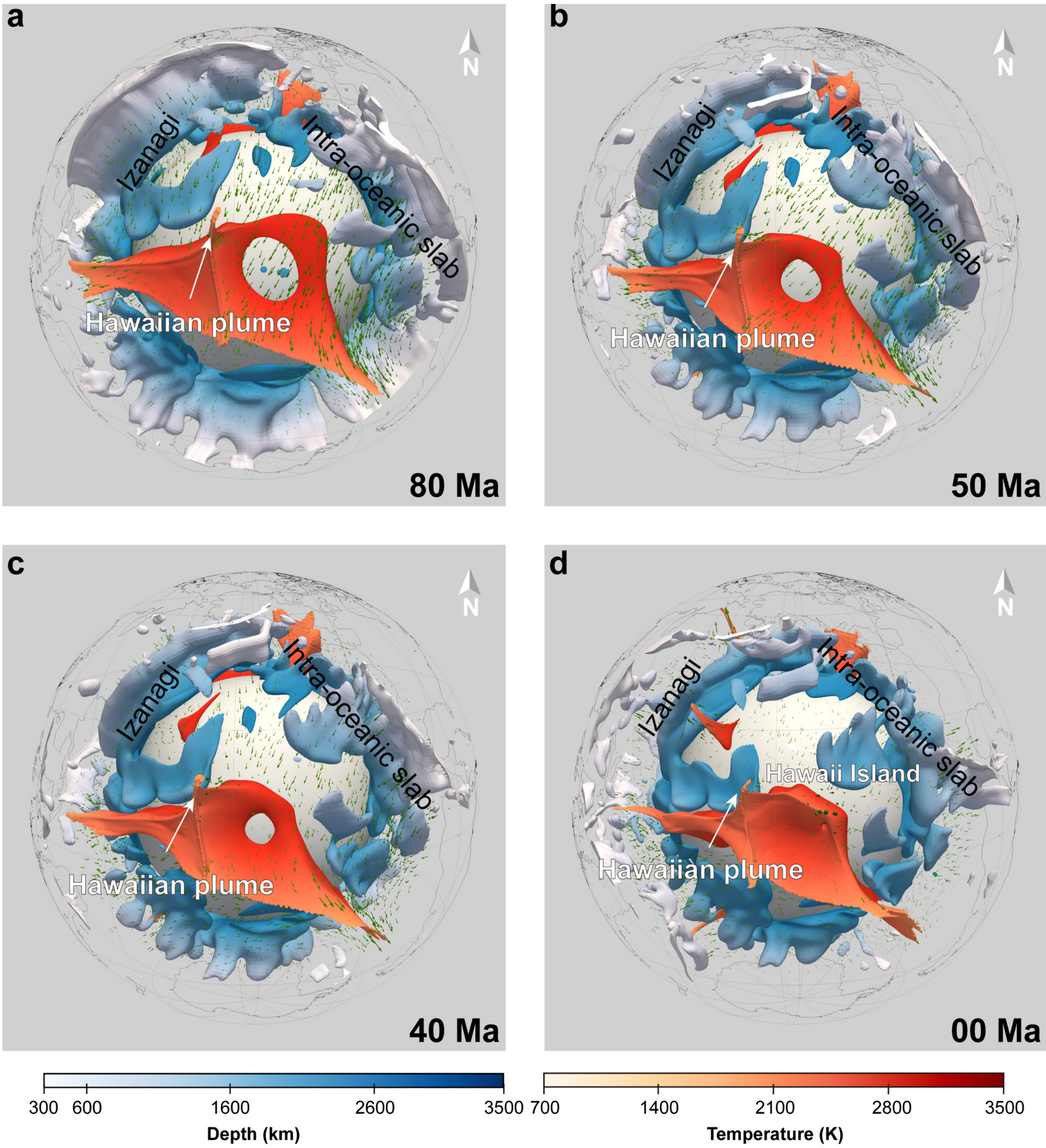

Fig.3. Evolution of the Hawaiian plume at 80 Ma (a), 50 Ma (b), 40 (c) and 0 Ma (d) for the reference model that incorporates the intraoceanic subduction in northeastern Pacific. Plume conduits delineated with temperature contours 420 K hotter than the ambient mantle (warm colors) and slabs delineated with temperature contours 300 K colder than the ambient mantle (cold colors) are shown for each panel. Mantle flow below 1000 km depth is shown with green arrows. The top 250 km of the domain is not rendered.

Formation of the Hawaiian-Emperor Bend

We compute the Hawaiian-Emperor Chain by combining the predicted trajectories of hotspot drift (Fig. 4; Extended Data Fig. 3; Extended Data Fig. 6; Extended Data Table 2) with the sudden change in Pacific Plate motion constrained by the geodynamic model of Hu et al. (2022)[11]. Utilizing the dominantly southward hotspot drift from the five comparison models that do not take into account the intraoceanic subduction west of North America, yields five distinct hotspot tracks, but they generally fail in fitting the observation (Extended Data Fig. 3a-e). These tracks possess an HEB angle that is much smaller than the observation. We have also considered hotspot drifting trajectory from previous study, including the one by Hassan et al. (2016)[7] (Extended Data Fig. 3f). The predicted HEB angle is insufficient to explain observation either. In contrast, models with northeastern Pacific intraoceanic subduction generally predict a larger angle of HEB (Extended Data Fig. 6), with the best-fit Hawaiian-Emperor Chain obtained using the hotspot drift trajectory taken from the reference model (Fig. 4). This predicted hotspot track is nearly identical to the observed Hawaiian-Emperor chain (Fig. 4a). The hotspot track experienced a significant bend at ~47 Ma, with a bending angle close to 60 degrees. Of this, the sudden change in direction of the Pacific Plate motion contributed 30-35 degrees[11], while the remaining 25-30 degrees resulted from the drift of the Hawaiian hotspot. Note that the geodynamic model of Hu et al. (2022)[11] attributes the change in Pacific Plate motion to the termination of the Kronotsky intraoceanic subduction in northern Pacific at 47 Ma, which is also incorporated by our reference model. In other words, although the hotspot drift trajectory and the Pacific Plate motion are derived from two different types of geodynamic models, they are largely consistent in terms of the plate configuration they use.

To untangle the influence of the longitudinal and latitudinal drift on the formation of the HEB, we divide the hotspot track into two phases: a southwestward drift between 85-45 Ma and a southeastward drift after 45 Ma, then separately test the effects of the longitudinal motion of each phase (Fig. 4d-f). We first examine the hotspot track without longitudinal drift and with only north-south drift (Fig. 4d). In this scenario, the hotspot track exhibits a bend of approximately 40°, primarily caused by the steering of the Pacific plate. Subsequently, we conducted tests that further consider the presence of the westward drift before 45 Ma (Fig. 4e) and the eastward drift after 45 Ma (Fig. 4f). The former yields a hotspot track that is very similar to our best-fit track with very minor difference for the Hawaiian Chain that tends to reduce the angle of the HEB, while the latter yields a poor fit to the observed Hawaiian-Emperor Chain and an HEB of ~40°. These comparison tests reveal that the westward drift of the hotspot before the bend has an approximately 20° effect on the angle of the HEB, while the eastward drift after the bend contributes positively but also marginally to the angle of the HEB. We have done a similar analysis to isolate the effect of southward hotspot motion (Extended Data Fig. 8). Although the southward hotspot motion is absolutely important in fitting the Emperor Chain, it has a secondary contribution to the angle between the Hawaiian Chain and the Emperor Chain (Extended Data Fig. 8). This suggests that the westward motion indeed has a larger contribution to the angle of the HEB.

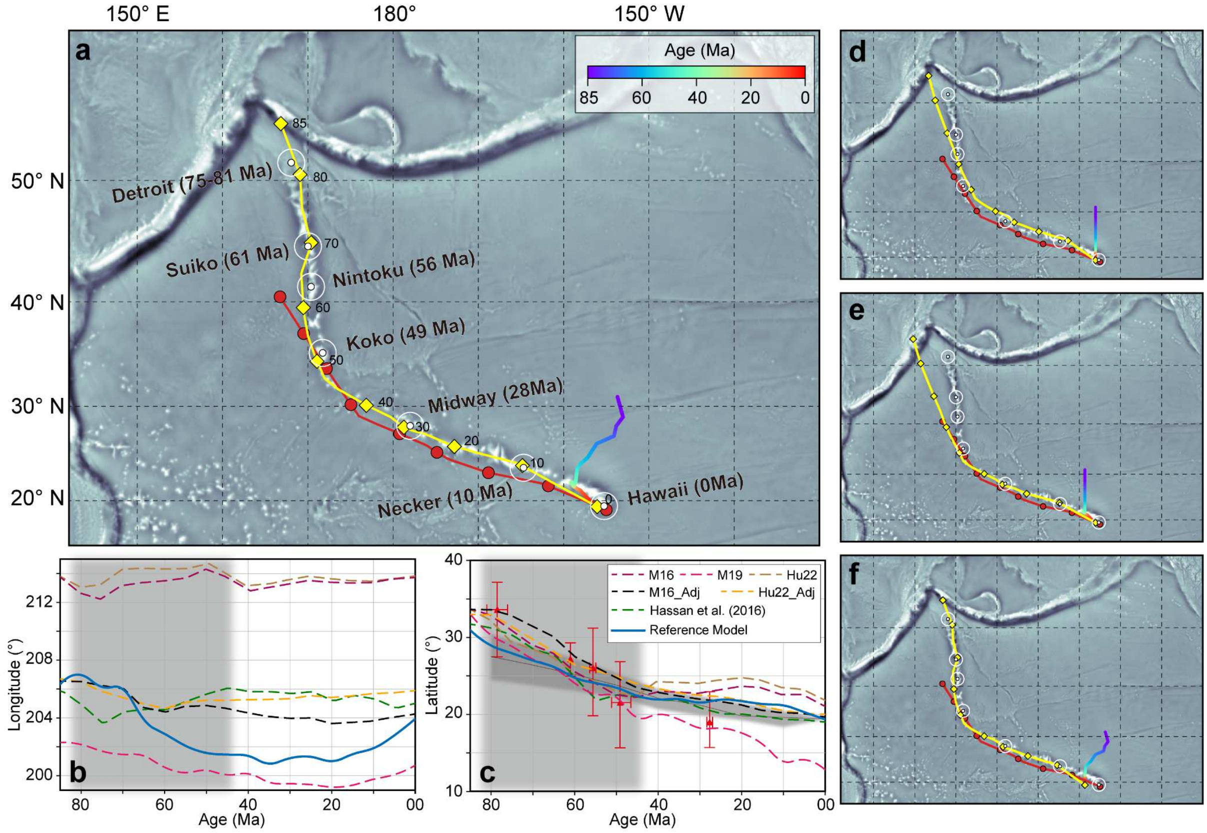

Fig. 4. Predicted hotspot tracks. a, The multicoloured trajectory represents the motion of the Hawaiian plume at a depth of 300 km in the reference model. The red line indicates the Pacific Plate motion track proposed by Hu et al. (2022)[11], with the red circles marking the 10-Myr intervals. The yellow line represents the predicted hotspot track, with the yellow diamonds along the hotspot track marking the 10-Myr intervals. **b**, The colored lines show predicted paleolongitudes of the Hawaiian hotspots in the reference model, comparison models and

Hassan et al. (2016)[7]. **c**, The colored lines show predicted palaeolatitudes of the Hawaiian hotspots in the reference model, comparison models and Hassan et al. (2016)[7], which are compared against latitudinal estimates of surface motions of the Hawaiian hotspot after Doubrovine et al. (2012)[29] (thick black line with grey-shaded 95% confidence region) and the palaeomagnetic results by Tarduno et al. (2003)[4] (red thin lines with 95% confidence bars). **d-f**, Testing the impact of longitudinal hotspot motion on the predicted track (**d**: lack of longitudinal motion, **e**: no westward drift before HEB, **f**: no eastward drift after HEB).

Implications

The westward hotspot drift components predicted by our models are always smaller than 15° (Extended Data Fig. 6), even when the intraoceanic subduction in northeastern Pacific has already been considered and a wide range of model parameters have been explored (Models 2-9 in Extended Data Table 2). This suggests that the Pacific Plate motion change at 47 Ma is required to fit the HEB (Fig. 1), consistent with recent plate reconstructions[13,16,30] and high-resolution global geodynamic prediction[11]. Very interestingly, the hotspot drift trajectories predicted by models with intraoceanic subduction show a sudden slow down or a stop of westward drift also around 47 Ma (Fig. 4a, b; Extended Data Fig. 6), implying a causal relationship between the two events. We contend that the change in Pacific Plate motion might be the trigger for the change in hotspot drift. When the Pacific Plate motion changed from north-northwest to west-northwest, a compensate southeastward mantle flow would form in the lower mantle[11], as demonstrated by both models with and without the intraoceanic subduction in northeastern Pacific at 40 Ma (Extended Data Fig. 4; Extended Data Fig. 7). For the comparison model that does not incorporate the intraoceanic subduction, this does not induce much change in the lower mantle flow as the southeastward flow dominates in central Pacific even before the bend (Extended Data Fig. 4), while for the reference model, this causes a strong change in mantle flow, from dominantly southwestward to southeastward (Extended Data Fig. 7). This strongly suggests that the plate and the mantle are a coupled system - any plate reorganization events should also be accompanied by reorganization of the deep mantle flow.

Our models have important implications on the source of the Hawaiian plume. Seismological studies have attributed the location of the Hawaiian plume root to either the southeastern side or the southwestern side of the Hawaiian Islands, but no consensus has been reached. For example, waveform analyses have revealed the presence of a significant mega-ULVZ, referred to as the Hawaiian mega-sized ULVZ[31] or North Pacific ULVZ[32], on the southwestern side of the Hawaiian Islands[31–33]; while several patchy ULVZs have been observed on the southeastern side[34–39] (Fig. 5). Both have been attributed to the source of the Hawaiian plume. Thinning of the mantle transition zone indicating potential traverse of plume has been observed on both the southwestern side[40,41] and the southeastern side[42]. Additionally, tomographic imaging has suggested both a southwestward dipping[43–45] or a southeastward dipping Hawaiian plume[46] that extends down to the lower mantle. These results indicate the significant challenge in mapping the Hawaiian plume root. Our model serves as an additional constraint for the plume root. In our reference model, the southwestward motion dominates the Hawaiian plume motion, causing the final position of the Hawaiian plume root to be located to the southwest of the Hawaii Islands (Fig. 3d; Fig. 5), in contrast to the prediction by Hassan et al. (2016)[7] which shows a southeastward plume drifting and locates the plume root to the southeastern side. This suggests that our models are eventually testable, as the plume drifting process and the final location of the plume root are coupled. Since a southwestward hotspot drift is required to fit the HEB (Fig. 1), we contend that the current Hawaiian plume root is located on the southwestern side of the Hawaiian Islands.

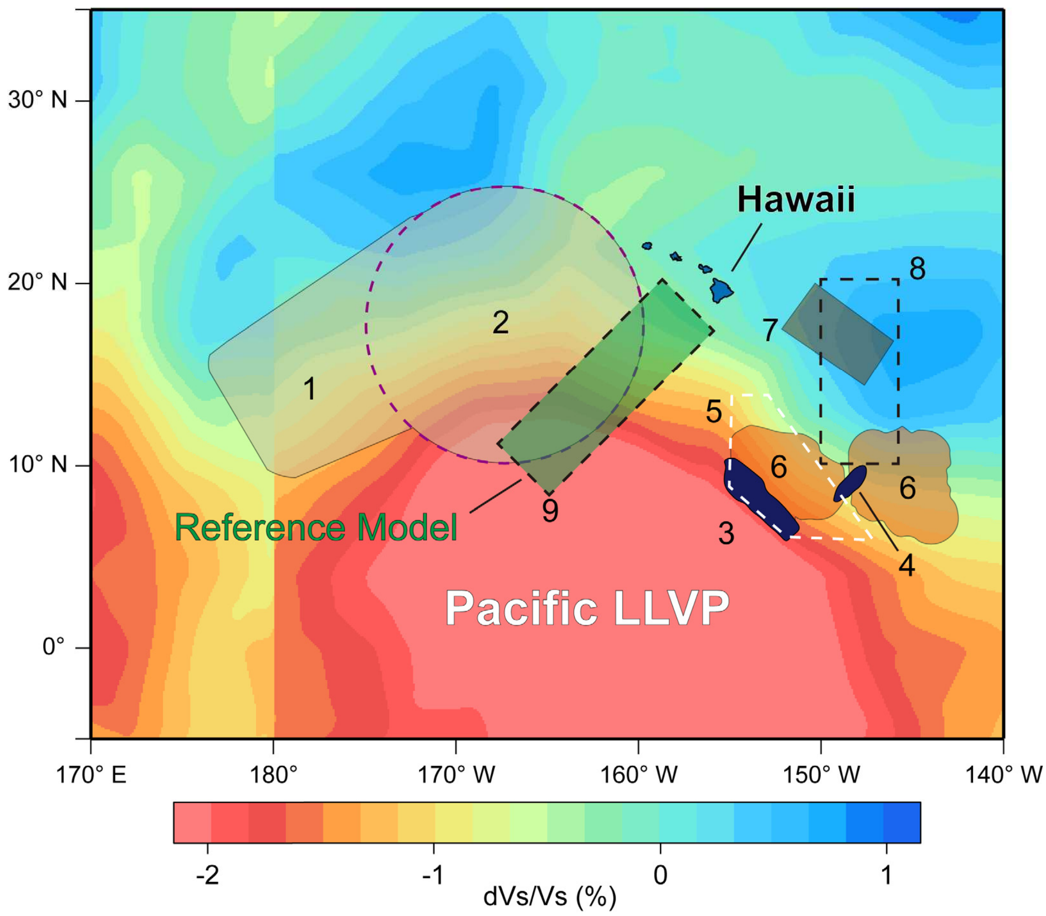

Fig. 5. Hawaiian plume root and Distribution of ULVZs. The shadow region and colored dashed lines indicate the ULVZs: 1 represents North Pacific ULVZ[32], 2 represents Hawaiian mega-sized ULVZ[31], 3[34–36], 4[37], 5[36], 6[39], 7[38]. The black dash lines indicate the plume root from numerical modeling: 8[7], 9 from our reference model. The background tomography image is from the GyPSuM[47] at the core-mantle boundary.

Acknowledgements

J.H. and J.Z. are supported by the National Natural Science Foundation of China (NSFC) through awards 42174106 and 92155307, and the National Key R&D Program of China through awards 2023YFF0806300 and 2023YFF0803200. Computations were carried out at the Center for Computational Science and Engineering at Southern University of Science and Technology.

Author contributions

J.H. conceived the study and designed the initial model. J.Z. performed the numerical experiments and processed the results. Both authors participated in result interpretation and manuscript preparation.

Competing interests

The authors declare no competing interests.

Code availability

The computational code CitcomS is available at www.geodynamics.org/cig/software/citcoms/. The plate kinematic tool GPlates and its python version can be accessed at www.gplates.org/.

Data availability

Data generated in this study are available within the paper. Source data are provided with this paper.

Additional information

Extended data is available for this paper

References

1. Wilson, J. T. Evidence from ocean islands suggesting movement in the earth. *Philosophical Transactions of the Royal Society of London. Series A, Mathematical and Physical Sciences* **258**, 145–167 (1965).
2. Morgan, W. J. Deep mantle convection plumes and plate motions. *AAPG bulletin* **56**, 203–213 (1972).
3. Torsvik, T. H. *et al.* Pacific plate motion change caused the Hawaiian-Emperor Bend. *Nature Communications* **8**, 15660 (2017).
4. Tarduno, J. A. *et al.* The Emperor Seamounts: Southward motion of the Hawaiian hotspot plume in Earth's mantle. *Science* **301**, 1064–1069 (2003).
5. Steinberger, B., Sutherland, R. & O'connell, R. J. Prediction of Emperor-Hawaii seamount locations from a revised model of global plate motion and mantle flow. *Nature* **430**, 167–173 (2004).
6. Tarduno, J. A., Bunge, H. P., Sleep, N. & Hansen, U. The bent Hawaiian-Emperor hotspot track: Inheriting the mantle wind. *Science* **324**, 50–53 (2009).

7. Hassan, R., Müller, R. D., Gurnis, M., Williams, S. E. & Flament, N. A rapid burst in hotspot motion through the interaction of tectonics and deep mantle flow. *Nature* **533**, 239–242 (2016).

8. Konrad, K. *et al.* On the relative motions of long-lived Pacific mantle plumes. *Nature Communications* **9**, 854 (2018).

9. Bono, R. K., Tarduno, J. A. & Bunge, H.-P. Hotspot motion caused the Hawaiian-Emperor Bend and LLSVPs are not fixed. *Nature communications* **10**, 3370 (2019).

10. Sun, W. *et al.* Plume-ridge interaction induced migration of the Hawaiian-Emperor seamounts. *Science Bulletin* **66**, 1691–1697 (2021).

11. Hu, J., Gurnis, M., Rudi, J., Stadler, G. & Müller, R. D. Dynamics of the abrupt change in Pacific Plate motion around 50 million years ago. *Nature Geoscience* **15**, 74–78 (2022).

12. Jiang, Z. *et al.* The trials and tribulations of the Hawaii hot spot model. *Earth-Science Reviews* **215**, 103544 (2021).

13. Müller, R. D. *et al.* A global plate model including lithospheric deformation along major rifts and orogens since the Triassic. *Tectonics* **38**, 1884–1907 (2019).

14. Seton, M. *et al.* Global continental and ocean basin reconstructions since 200 Ma. *Earth-Science Reviews* **113**, 212–270 (2012).

15. Engebretson, D. C., Cox, A. & Gordon, R. G. Relative motions between oceanic and continental plates in the Pacific basin. (1985).

16. Müller, R. D. *et al.* Ocean basin evolution and global-scale plate reorganization events since Pangea breakup. *Annual Review of Earth and Planetary Sciences* **44**, 107–138 (2016).

17. Hu, J., Liu, L. & Zhou, Q. Reproducing past subduction and mantle flow using high-

resolution global convection models. *Earth and Planetary Physics* **2**, 189–207 (2018).

18. Clennett, E. J. *et al.* A quantitative tomotectonic plate reconstruction of western North America and the eastern Pacific basin. *Geochemistry, Geophysics, Geosystems* **21**, e2020GC009117 (2020).
19. Coney, P. J., Jones, D. L. & Monger, J. W. H. Cordilleran suspect terranes. *Nature* **288**, 329–333 (1980).
20. Silberling, N. J., Jones, D. L., Monger, J. W. H. & Coney, P. J. *Lithotectonic Terrane Map of the North American Cordillera*. (1992).
21. Moores, E. Ultramafics and orogeny, with models of the US Cordillera and the Tethys. *Nature* **228**, 837–842 (1970).
22. Ingersoll, R. V. & Schweickert, R. A. A plate-tectonic model for Late Jurassic Ophiolite Genesis, Nevadan orogeny and forearc initiation, northern California. *Tectonics* **5**, 901–912 (1986).
23. Moores, E. M. Ophiolites, the Sierra Nevada,“Cordilleria,” and orogeny along the Pacific and Caribbean margins of North and South America. *International Geology Review* **40**, 40–54 (1998).
24. Dickinson, W. R. Evolution of the North American cordillera. *Annu. Rev. Earth Planet. Sci.* **32**, 13–45 (2004).
25. Dickinson, W. R. Accretionary Mesozoic–Cenozoic expansion of the Cordilleran continental margin in California and adjacent Oregon. *Geosphere* **4**, 329–353 (2008).
26. Ingersoll, R. V. Subduction-related sedimentary basins of the USA Cordillera. *Sedimentary basins of the world* **5**, 395–428 (2008).

27. Sigloch, K. & Mihalynuk, M. G. Intra-oceanic subduction shaped the assembly of Cordilleran North America. *Nature* **496**, 50–56 (2013).

28. Sigloch, K. & Mihalynuk, M. G. Mantle and geological evidence for a Late Jurassic–Cretaceous suture spanning North America. *GSA Bulletin* **129**, 1489–1520 (2017).

29. Doubrovine, P. V., Steinberger, B. & Torsvik, T. H. Absolute plate motions in a reference frame defined by moving hot spots in the Pacific, Atlantic, and Indian oceans. *Journal of Geophysical Research: Solid Earth* **117**, (2012).

30. Torsvik, T. H. *et al.* Pacific-Panthalassic reconstructions: Overview, errata and the way forward. *Geochemistry, Geophysics, Geosystems* **20**, 3659–3689 (2019).

31. Cottaar, S. & Romanowicz, B. An unsually large ULVZ at the base of the mantle near Hawaii. *Earth and Planetary Science Letters* **355**, 213–222 (2012).

32. Li, J., Sun, D. & Bower, D. J. Slab control on the mega-sized North Pacific ultra-low velocity zone. *Nature Communications* **13**, 1042 (2022).

33. Jenkins, J., Mousavi, S., Li, Z. & Cottaar, S. A high-resolution map of Hawaiian ULVZ morphology from ScS phases. *Earth and Planetary Science Letters* **563**, 116885 (2021).

34. Avants, M., Lay, T. & Garnero, E. J. A new probe of ULVZ S-wave velocity structure: Array stacking of ScS waveforms. *Geophysical Research Letters* **33**, (2006).

35. Hutko, A. R., Lay, T. & Revenaugh, J. Localized double-array stacking analysis of PcP: D ″and ULVZ structure beneath the Cocos plate, Mexico, central Pacific, and north Pacific. *Physics of the Earth and Planetary Interiors* **173**, 60–74 (2009).

36. Lay, T., Hernlund, J., Garnero, E. J. & Thorne, M. S. A post-perovskite lens and D”heat flux beneath the central Pacific. *science* **314**, 1272–1276 (2006).

37. Liu, L., Tan, Y., Sun, D., Chen, M. & Helmberger, D. Trans-Pacific whole mantle structure. *Journal of Geophysical Research: Solid Earth* **116**, (2011).

38. Sun, D. *et al.* Slab control on the northeastern edge of the mid-Pacific LLSVP near Hawaii. *Geophysical Research Letters* **46**, 3142–3152 (2019).

39. Zhao, C., Garnero, E. J., Li, M., McNamara, A. & Yu, S. Intermittent and lateral varying ULVZ structure at the northeastern margin of the Pacific LLSVP. *Journal of Geophysical Research: Solid Earth* **122**, 1198–1220 (2017).

40. Cao, Q., Van der Hilst, R. D., De Hoop, M. V. & Shim, S. H. Seismic imaging of transition zone discontinuities suggests hot mantle west of Hawaii. *science* **332**, 1068–1071 (2011).

41. Kemp, M., Jenkins, J., Maclennan, J. & Cottaar, S. X-discontinuity and transition zone structure beneath Hawaii suggests a heterogeneous plume. *Earth and Planetary Science Letters* **527**, 115781 (2019).

42. Schmerr, N., Garnero, E. & McNamara, A. Deep mantle plumes and convective upwelling beneath the Pacific Ocean. *Earth and Planetary Science Letters* **294**, 143–151 (2010).

43. Ye, C., Liu, X., Zhao, D. & Zhao, S. Robust seismic images of the Hawaiian plume. *Geophysical Research Letters* **49**, e2022GL100707 (2022).

44. Hosseini, K. *et al.* Global mantle structure from multifrequency tomography using P, PP and P-diffracted waves. *Geophysical Journal International* **220**, 96–141 (2020).

45. French, S. W. & Romanowicz, B. A. Whole-mantle radially anisotropic shear velocity structure from spectral-element waveform tomography. *Geophysical Journal International* **199**, 1303–1327 (2014).

46. Wolfe, C. J. *et al.* Mantle shear-wave velocity structure beneath the Hawaiian hot spot.

science **326**, 1388–1390 (2009).

47. Simmons, N. A., Forte, A. M., Boschi, L. & Grand, S. P. GyPSuM: A joint tomographic model of mantle density and seismic wave speeds. *Journal of Geophysical Research: Solid Earth* **115**, (2010).
48. Christensen, U. R. & Yuen, D. A. Layered convection induced by phase transitions. *Journal of Geophysical Research: Solid Earth* **90**, 10291–10300 (1985).
49. Zhong, S., McNamara, A., Tan, E., Moresi, L. & Gurnis, M. A benchmark study on mantle convection in a 3-D spherical shell using CitcomS. *Geochemistry, Geophysics, Geosystems* **9**, (2008).
50. Zhong, S. Constraints on thermochemical convection of the mantle from plume heat flux, plume excess temperature, and upper mantle temperature. *Journal of Geophysical Research: Solid Earth* **111**, (2006).
51. Leng, W. & Zhong, S. Controls on plume heat flux and plume excess temperature. *Journal of Geophysical Research: Solid Earth* **113**, (2008).
52. Tosi, N., Yuen, D. A., De Koker, N. & Wentzcovitch, R. M. Mantle dynamics with pressure- and temperature-dependent thermal expansivity and conductivity. *Physics of the Earth and Planetary Interiors* **217**, 48–58 (2013).
53. Hassan, R., Flament, N., Gurnis, M., Bower, D. J. & Müller, D. Provenance of plumes in global convection models. *Geochemistry, Geophysics, Geosystems* **16**, 1465–1489 (2015).
54. Karlsen, K. S., Domeier, M., Gaina, C. & Conrad, C. P. A tracer-based algorithm for automatic generation of seafloor age grids from plate tectonic reconstructions. *Computers & Geosciences* **140**, 104508 (2020).

55. Gurnis, M. *et al.* Plate tectonic reconstructions with continuously closing plates. *Computers & Geosciences* **38**, 35–42 (2012).

56. Faccenda, M., Gerya, T. V. & Burlini, L. Deep slab hydration induced by bending-related variations in tectonic pressure. *Nature Geoscience* **2**, 790–793 (2009).

57. Ishii, T. & Ohtani, E. Dry metastable olivine and slab deformation in a wet subducting slab. *Nature Geoscience* **14**, 526–530 (2021).

58. Čížková, H., van Hunen, J., van den Berg, A. P. & Vlaar, N. J. The influence of rheological weakening and yield stress on the interaction of slabs with the 670 km discontinuity. *Earth and Planetary Science Letters* **199**, 447–457 (2002).

59. Mohiuddin, A., Karato, S. & Girard, J. Slab weakening during the olivine to ringwoodite transition in the mantle. *Nature Geoscience* **13**, 170–174 (2020).

60. Gerya, T. V., Bercovici, D. & Becker, T. W. Dynamic slab segmentation due to brittle–ductile damage in the outer rise. *Nature* **599**, 245–250 (2021).

61. Flament, N., Bodur, Ö. F., Williams, S. E. & Merdith, A. S. Assembly of the basal mantle structure beneath Africa. *Nature* **603**, 846–851 (2022).

62. Ester, M., Kriegel, H. P., Sander, J. & Xu, X. A density-based algorithm for discovering clusters in large spatial databases with noise. in *kdd* vol. 96 226–231 (1996).

Methods

We conduct thermochemical convection models for the Earth's mantle using the extended-Boussinesq approximation[48] in a spherical shell. The mass, momentum, and energy conservation equations are solved using the finite element code CitcomS[49]. Our model domain consists of hexahedral meshes with approximately 12.6 million elements, featuring a uniform lateral resolution of around 23 km and a variable vertical resolution that becomes finer near the surface (~13 km) and the core-mantle boundary (~21 km). To simulate the actual history of subduction, our model incorporates progressive assimilation of the age of the ocean floor, as well as the location and polarity of subduction zones[17]. Viscous dissipation, an adiabatic temperature gradient, internal heating, and the depth-dependent coefficient of thermal expansion are considered in our models[50–53]. For a comprehensive list of parameters used, please refer to Extended Data Table 1.

Data assimilation: We assimilate four plate reconstructions (Müller et al. (2016)[16], Müller et al. (2019)[13], Hu et al. (2022)[11] and a revised reconstruction based on Clennett et al. (2020)[18]) as boundary conditions in our geodynamic models. In the case of the revised Clennett et al. (2020)[18] model, we have employed a tracer-based algorithm described in Karlsen et al.[54] to construct age grids of the seafloor (Fig. 2d-f). We extract plate motion data from these reconstructions using the GPlates (www.gplates.org)[55] and output at every Myr. Surface velocity conditions are interpolated between adjacent input conditions when model time step is much smaller than 1 Myr. The assimilation of plate motion is crucial for accurately matching the observed present-day slab geometry and associated mantle flow by ensuring proper subduction at the appropriate geographic location.

At each time step, we additionally assimilate and update the thermal structure of the lithosphere based on the reconstructed seafloor ages. In an oceanic lithosphere, we use half space cooling model to define its thermal structure:

$$T_l(z,t) = T_{\mathrm{p}}\mathrm{erf}\left(\frac{z}{2\sqrt{t\kappa}}\right), \tag{2}$$

where T_l is the temperature of the lithosphere, T_{p} is the mantle potential temperature, z is depth,

t is seafloor age taken from plate reconstructions, κ is thermal diffusivity. We use the same model to define the thermal structure of continental lithosphere but with an age of 50 Ma. The thin continental lithosphere here helps in prohibiting widespread lithospheric dripping, while having no influence on deep mantle dynamics. To guarantee that a smooth thermal profile translates from within the oceanic plates into the down-going slab, and to make sure that other plate boundary properties such as composition and viscosity could evolve self-consistently, we avoid updating the temperature of the subducting and overriding plates within 600 km horizontal distance from the trench.

Rheology: The viscosity of this model is depth-, temperature- and composition-dependent:

$$\eta = \eta_0(r) C \exp\left(\frac{E_\eta(r)}{RT} - \frac{E_\eta(r)}{RT_\mathrm{m}}\right), \quad (1)$$

where η is the viscosity, T is the temperature, η_0 is the background viscosity (show in the Extended Data Fig. 1), C is the compositional viscosity pre-factor, E_η is the activation energy, R = 8.31 J mol^{-1} K^{-1} is the universal gas constant, and T_m is the temperature of the ambient mantle. The activation energy is 436 kJ mol^{-1} in our reference model. Slab has independent activation energy of 81 kJ mol^{-1} in our reference model (Extended Data Table 2), lower than the rest of the mantle to account for various slab weakening mechanisms including slab hydration[56,57], plastic yielding[58] and grain size damage[59,60], etc. Viscosity variations are limited to the range from 1.0×10^{20} Pa s to 5.0×10^{23} Pa s.

Composition: In our models, the composition field has an impact on both density and viscosity. The compositional density anomaly is defined using the ratio method:

$$B = \Delta\rho_\mathrm{ch}/(\rho_0 \alpha_0 \Delta T), \quad (3)$$

where B is the buoyancy ratio, an input parameter that varies with different compositions, $\Delta\rho_\mathrm{ch}$ the compositional density anomaly, ρ_0 the reference density, α_0 the reference thermal expansivity, and ΔT the temperature contrast across the mantle (Extended Data Table 1). The compositional effect on viscosity is achieved through a multiplication factor that is a geometric mean for all the compositions within the element:

$$C = \prod C_i^{r_i}, \quad (4)$$

where C is a prefactor, C_i is the viscosity multiplier for composition i, and r_i is the fraction of composition i over the total elemental composition. We assume chemical layering in the oceanic lithosphere to better simulate the subduction process. Within the oceanic plates, we define two distinct chemical layers that differ from the surrounding mantle: a crustal-viscosity layer and a crustal-density layer. The crustal-viscosity layer occupies the uppermost part of the oceanic plate and has an approximate thickness of 25 km. This layer is neutrally buoyant with a viscosity of 1.0×10^{20} Pa s when it subducts, thus acting as a lubricating layer to decouple the subducting plate from the overriding plate. In addition, we incorporate a crustal-density layer with neutral viscosity within the oceanic plates to accurately consider the buoyancy of the oceanic crust. This layer undergoes a phase change to eclogite at a depth of 80 km. We avoid updating the corresponding composition in the vicinity of the trench, such that tracer-carried properties (density and viscosity) will behavior naturally over time. In the initial time step, we introduce a uniform thermal-chemical layer located above the core-mantle boundary. This layer has a thermal thickness of 125 km and a compositional thickness of 100 km, similar to the approach described in Flament et al. (2022)[61]. The thermal-chemical layer possesses a neutral compositional viscosity and exhibits a positive density anomaly, with the corresponding buoyancy ratio listed in Extended Data Table 2.

Predict hotspot track: The hotspot detection in this study utilizes the Density-Based Spatial Clustering of Applications with Noise (DBSCAN) algorithm[62]. DBSCAN is a non-parametric density-based clustering algorithm that operates by grouping together points that are densely packed (having many nearby neighbors), while identifying outliers as points that exist in sparsely populated regions (with distant nearest neighbors). The algorithm relies on two parameters, namely ε and *MinPts*, to define the proximity characteristics of the data distribution. ε represents the neighborhood distance threshold (radius) for each data point, while *MinPts* specifies the minimum number of data points within a neighborhood with a radius ε from the given data point.

To identify the location of hotspots, the vertical velocity data at a depth of 300 km from the model is analyzed. Specifically, the data is output at regular intervals of 50 timesteps, and any velocity values exceeding 7 cm/yr upward are retained with their longitudes and latitudes, as they represent the upwelling mantle plume near the earth surface. Subsequently, the DBSCAN clustering algorithm is employed to these pairs of longitudes and latitudes, with the clustering parameters ε and *MinPts* set to 10 and 3, respectively. This enables the identification of hotspots by clustering the filtered vertical velocity data based on their proximity and density.

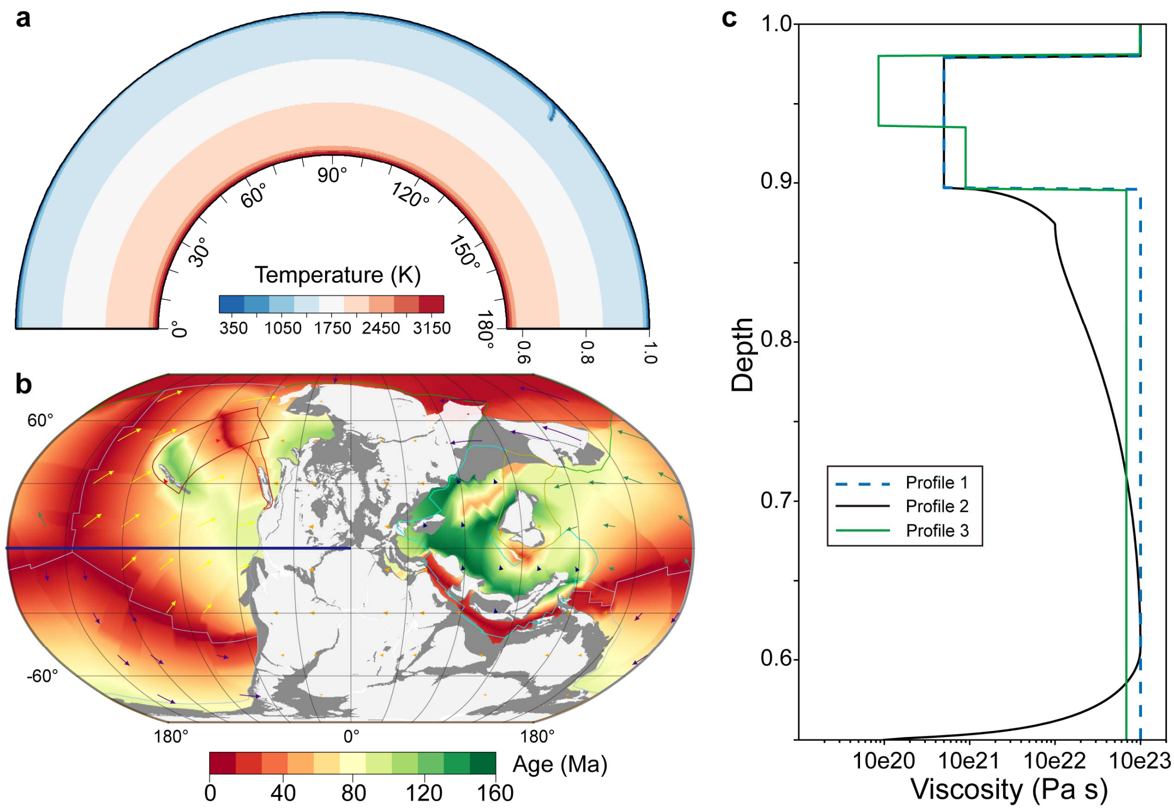

Extended Data Fig. 1. Initial conditions of the models. a, Mantle temperature along the cross-section shown in **b**. **b**, Imposed seafloor age at 250 Ma from Müller et al. (2019)[13]. The background color represents the seafloor age. Continents are shown in gray, the black lines show the plate boundary, the purple line is the location of the cross-section shown in **a**. **c**, Horizontally averaged initial mantle viscosity. Four different radial viscosity profiles are applied in our models. See details at Extended Data Table 2.

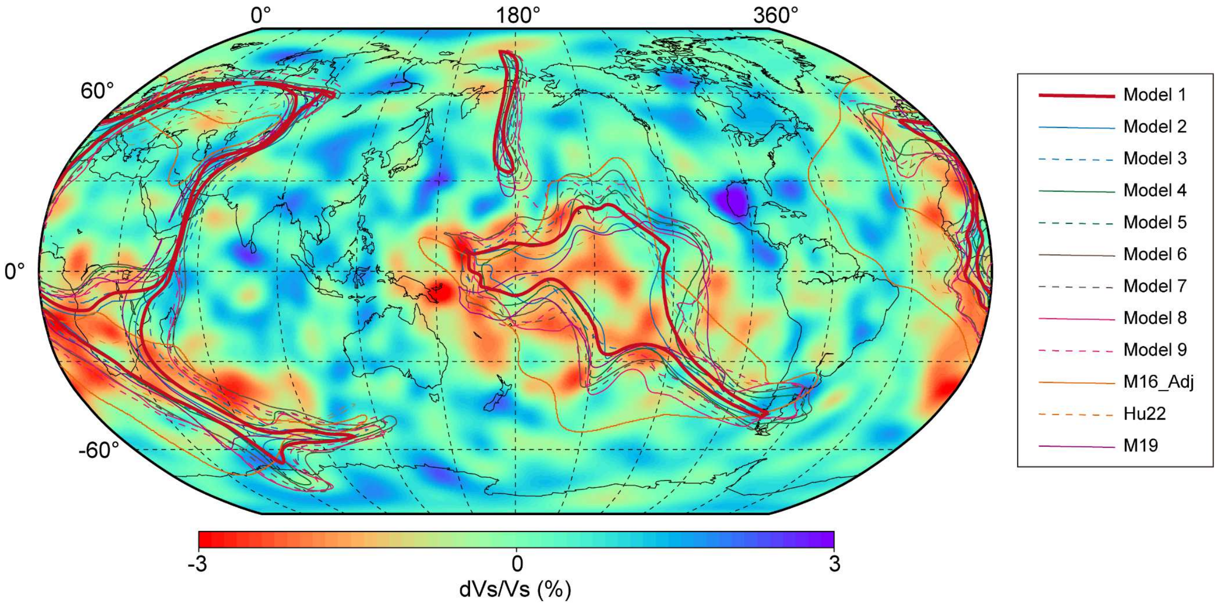

Extended Data Fig. 2. Comparison of model-predicted LLVPs with tomography. The background color represents shear velocity (Vs) perturbations at 2800 km depth from the SEMUCB-WM1 tomography model[45]. Contours show the 0.1 (350 K) temperature anomaly isosurface at the CMB from mantle flow models, representing the present-day shapes of the predicted LLVPs (Extended Data Table 2).

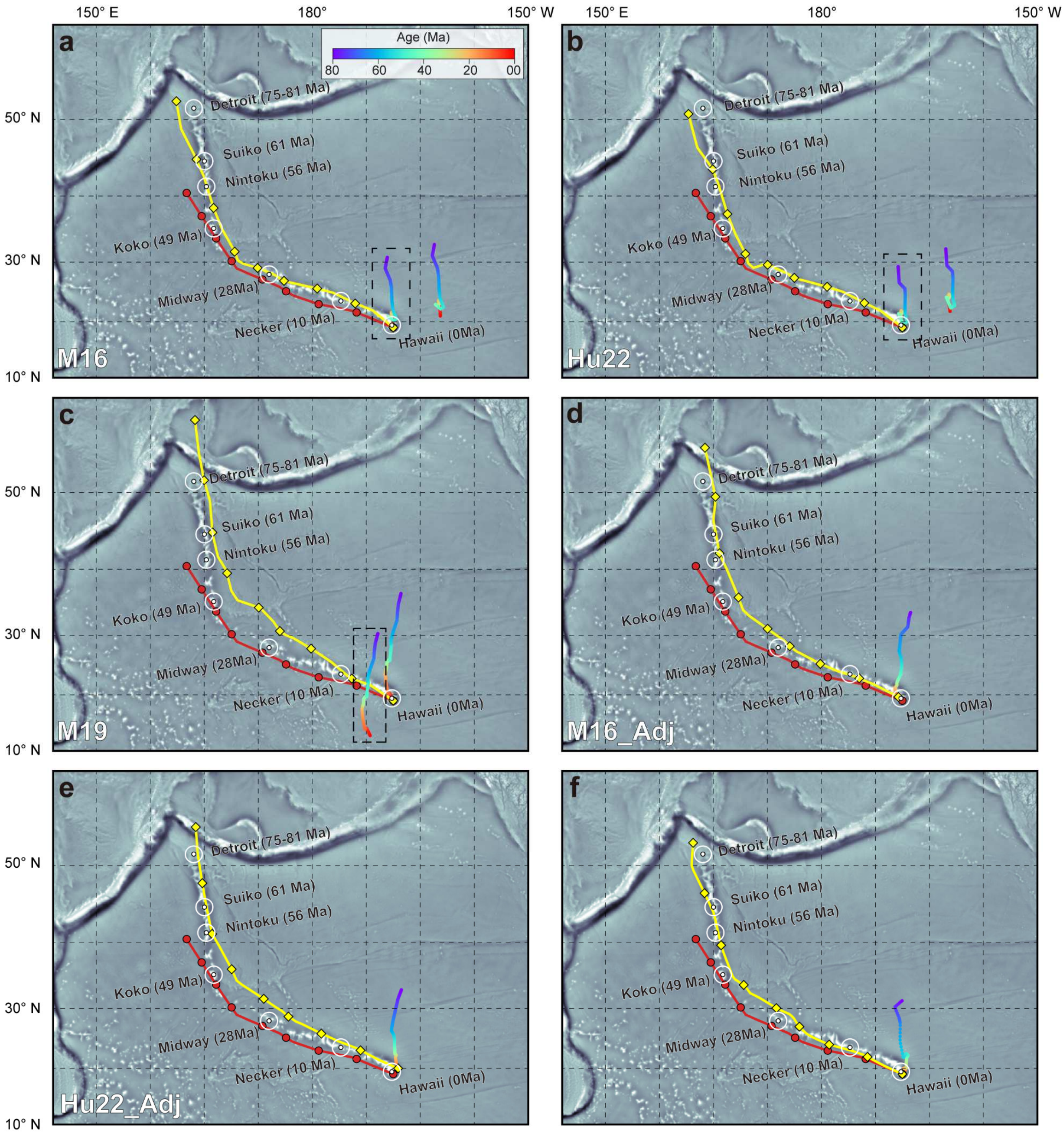

Extended Data Fig. 3. Predicted hotspot drift trajectories and hotspot tracks by different geodynamic models. a-c, The trajectories of the hotspots and predicted tracks derived from the comparison models of M16, Hu22 and M19. The dashed boxes outline the hotspot trajectories after translation to match the present-day location, which are further used to compute the hotspot tracks. **d-e**, The hotspot drift trajectories and predicted tracks derived from modifying the viscosity and density parameters of the comparison models M16 ("M16_Adj") and Hu22 ("Hu22_Adj"). Detailed information regarding these specific parameters can be found in Extended Data Table 2. **f**, Predicted hotspot track using the hotspot drift trajectory from Hassan et al. (2016)[7]. The assumed Pacific Plate motion follows the geodynamic model of Hu et al. (2022)[11], and is denoted by red lines with the red circles marking the 10-Myr intervals. The yellow lines represent predicted surface hotspot tracks, with the yellow diamonds along these hotspot tracks marking the 10-Myr intervals, The background shows gravity anomaly to reveal the Hawaiian–Emperor seamount chain.

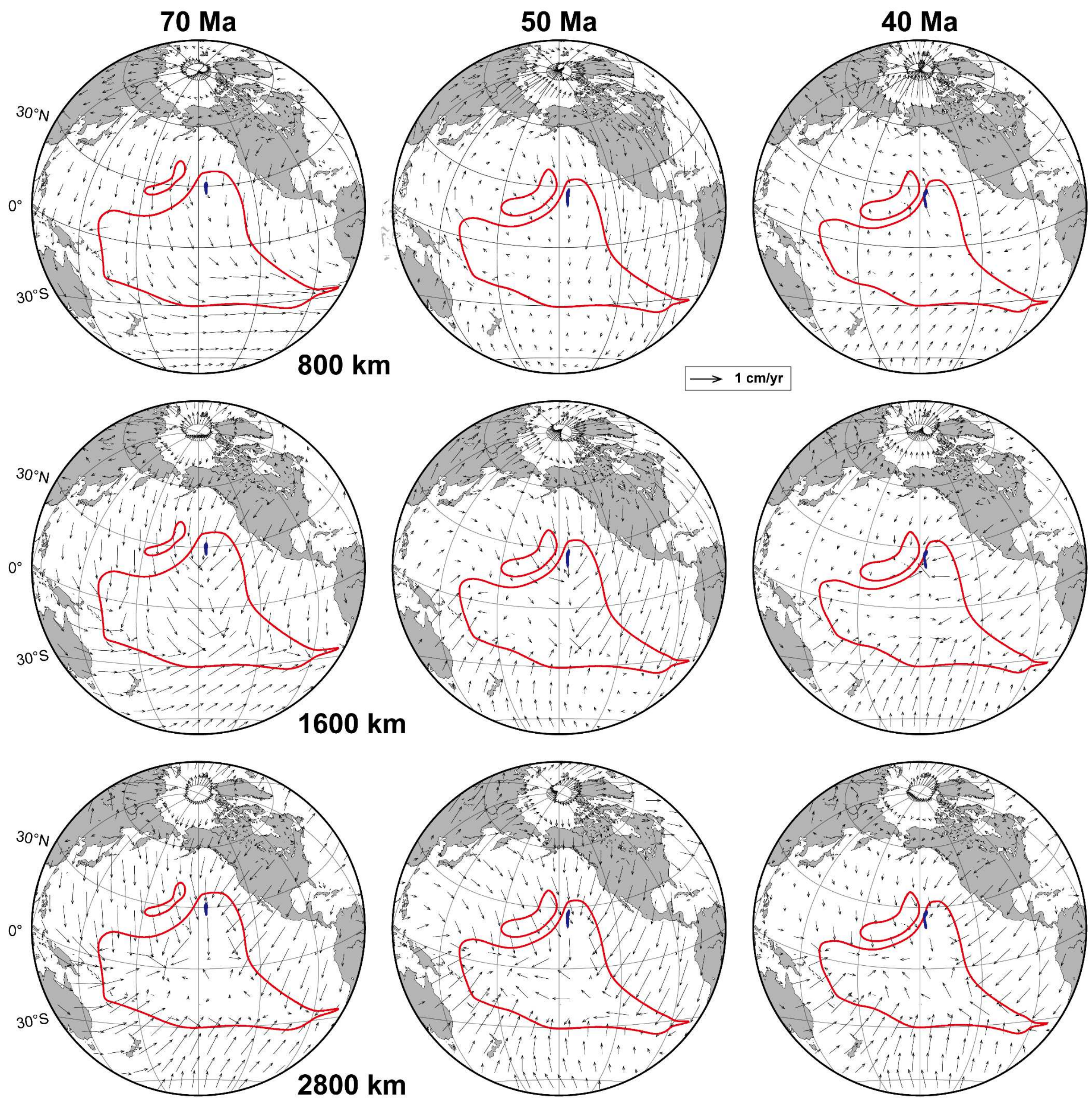

Extended Data Fig. 4. Temporal and spatial variation of the lower mantle flow field in the comparison model Hu22. Prior to the HEB (at 70 Ma, 50 Ma), the mantle flow originating from the northeast region converges with the mantle flow from the northwest in the central North Pacific. This convergence gives rise to a coherent southward flow field, which propels the thermochemical pile and Hawaiian plume towards the south (similar to Hassan et al. (2016)[7]). The thermochemical structural (LLVP) at the depth of 2800 km is outlined by the red solid line, while the extent of the mantle plume, characterized by a temperature anomaly of 0.1 (350 K) at 300 km, is represented by the blue dots. Columns from left to right show the mantle flow field at 70, 50 and 40 Ma; rows from top to bottom show the mantle low field at 800, 1600, and 2800 km depth.

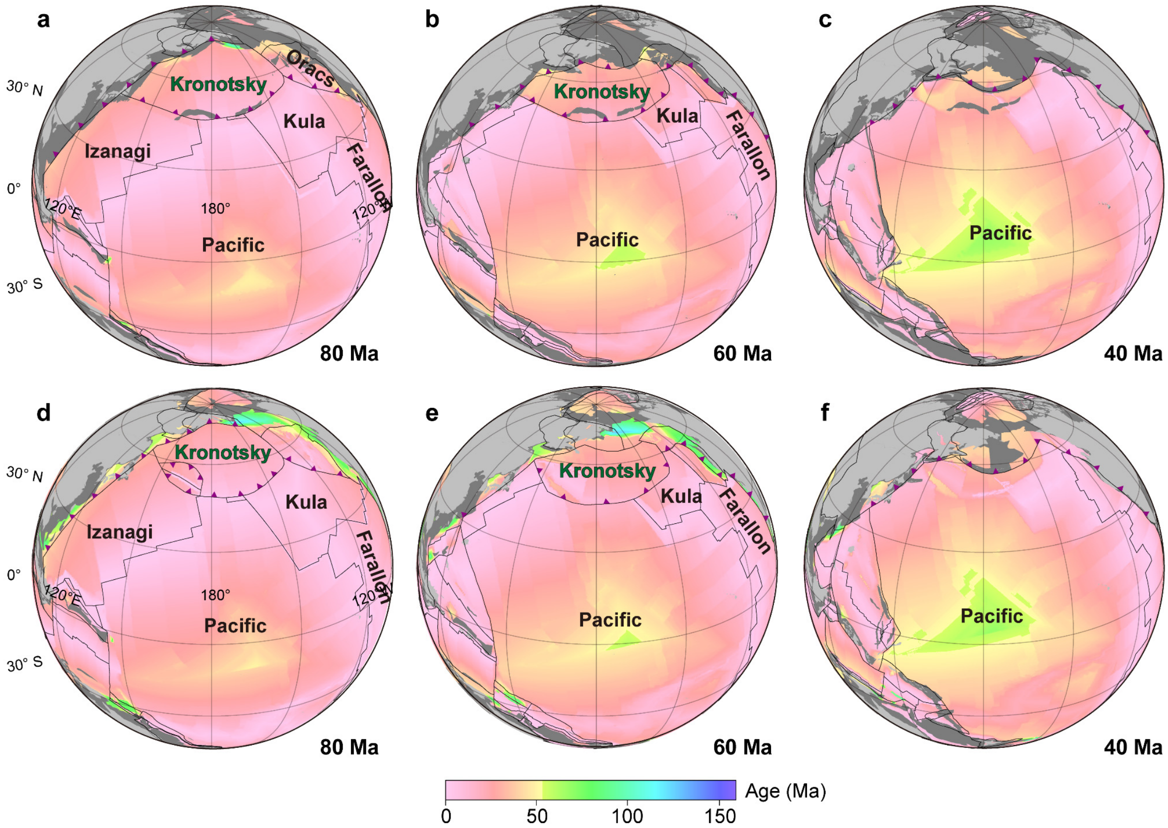

Extended Data Fig. 5. Global plate reconstructions from Late Cretaceous to Eocene, **a-c**, Unmodified Clennett et al. (2020)[18] plate reconstruction model. **d-f**, The plate reconstruction of Clennett et al. (2020)[18] that incorporates a revised Kronotsky intraoceanic subduction proposed by Hu et al. (2022)[11] in the northern Pacific.

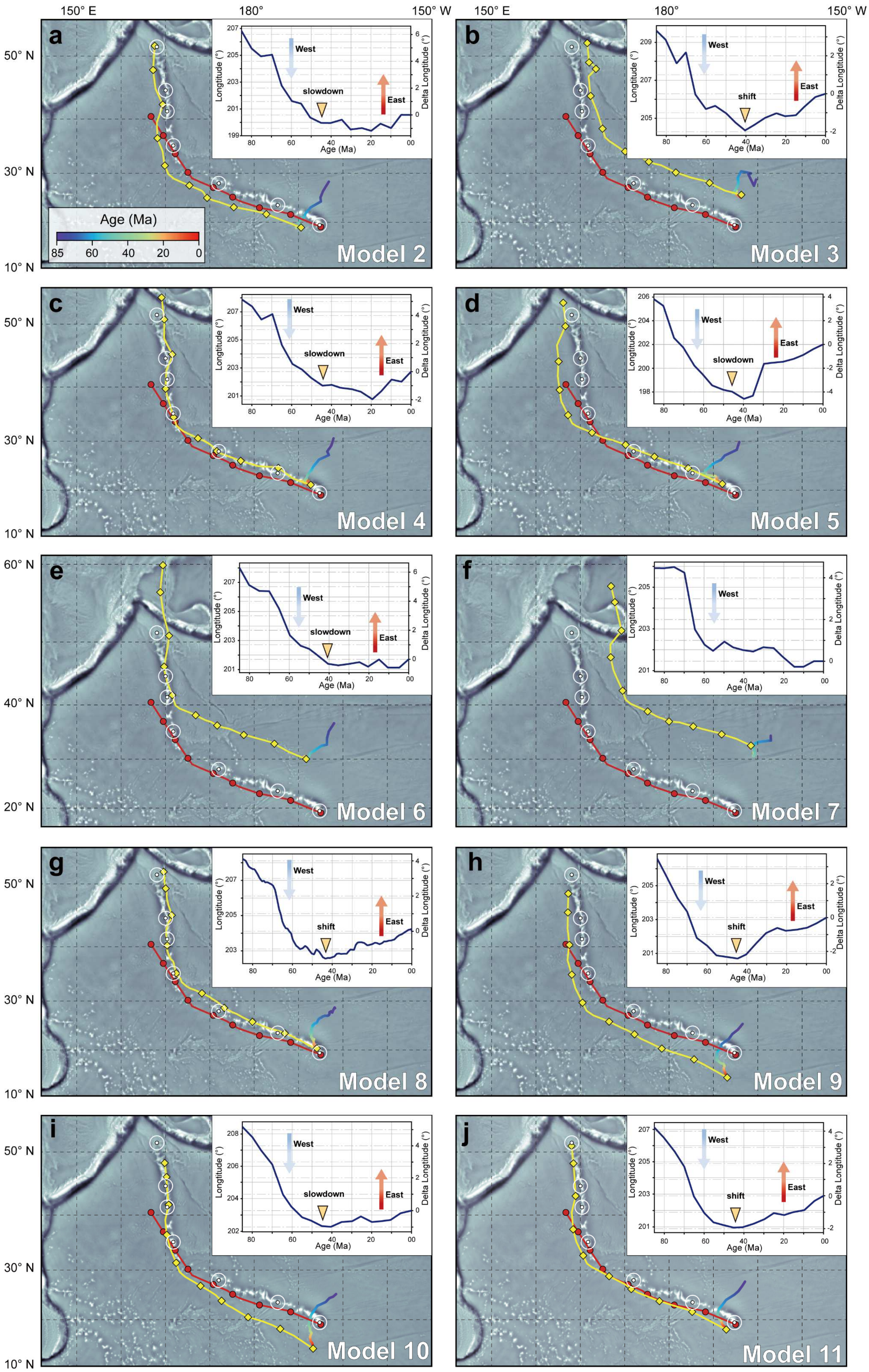

150° E
180°
150° W
50° N
30° N
10° N
60° N
40° N
20° N
a
b
c
d
e
f
g
h
i
j
Age (Ma)
85
60
40
20
0
West
East
slowdown
shift
Longitude (°)
Delta Longitude (°)
Age (Ma)
Model 2
Model 3
Model 4
Model 5
Model 6
Model 7
Model 8
Model 9
Model 10
Model 11

Extended Data Fig. 6. Predicted hotspot trajectories of the comparison models that use the same boundary conditions as the reference model. Symbols and legends are the same as Extended Data Fig. 3. The detailed parameters of different models can be seen in Extended Data Table 2. The inserted graphs show the longitudinal motion of the hotspots at 300 km depth. The yellow triangles mark the slowdown of the westward motion or the shift from westward motion to eastward motion.

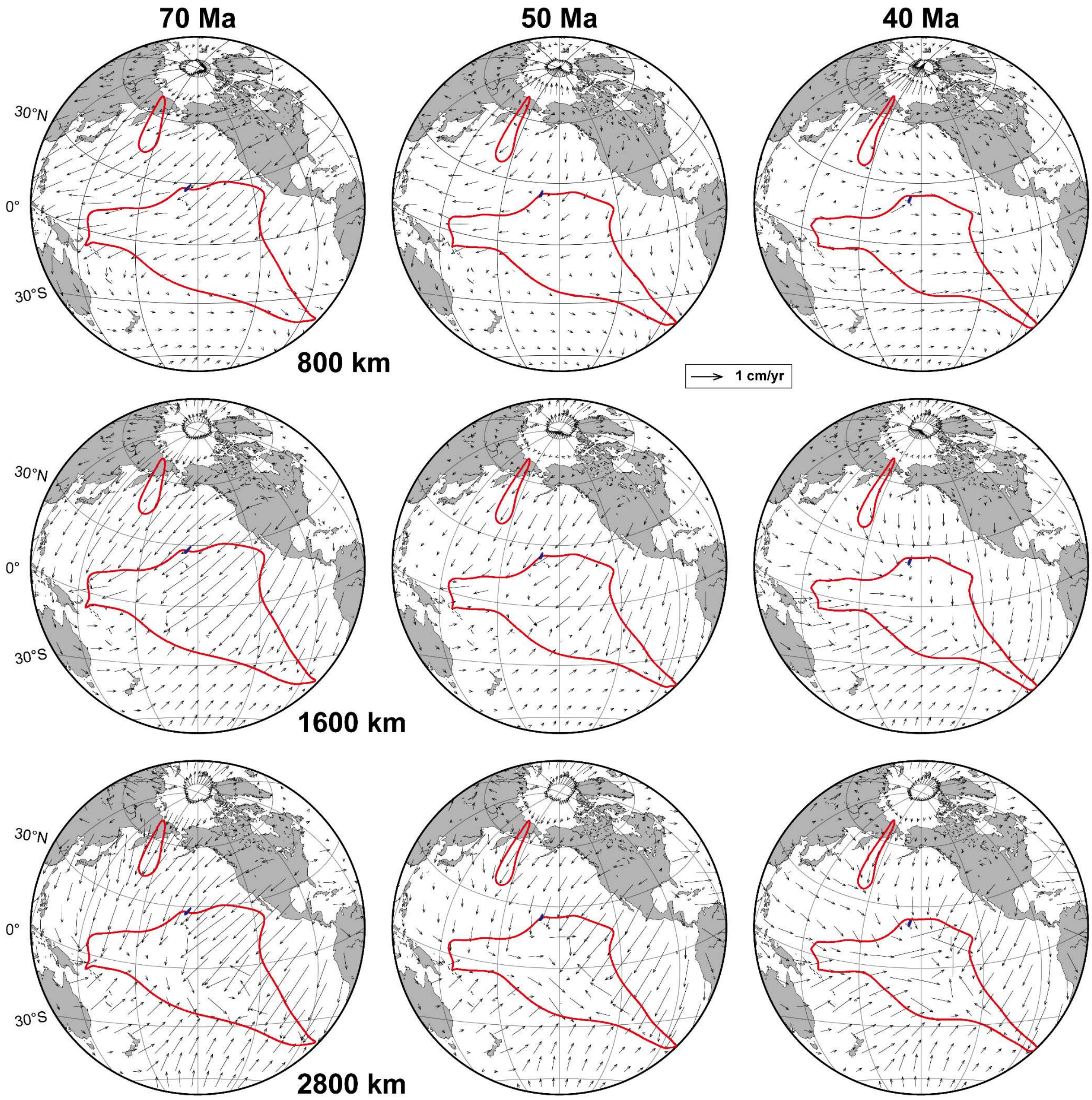

Extended Data Fig. 7. Temporal and spatial variation of the lower mantle flow field in the reference model. Prior to the HEB (at 70 Ma, 50 Ma), a notable southwestward flow field existed in the northeast Pacific Ocean, impacting both the thermochemical structural and the southwestward motion of the mantle plume. The thermochemical structural (LLVP) at the depth of 2800 km is outlined by the red solid line, while the extent of the mantle plume, characterized by a temperature anomaly of 0.1 (350 K) at 300 km, is represented by the blue dots. Columns from left to right show the mantle flow field at 70, 50 and 40 Ma; rows from top to bottom show the mantle low field at 800, 1600, and 2800 km depth.

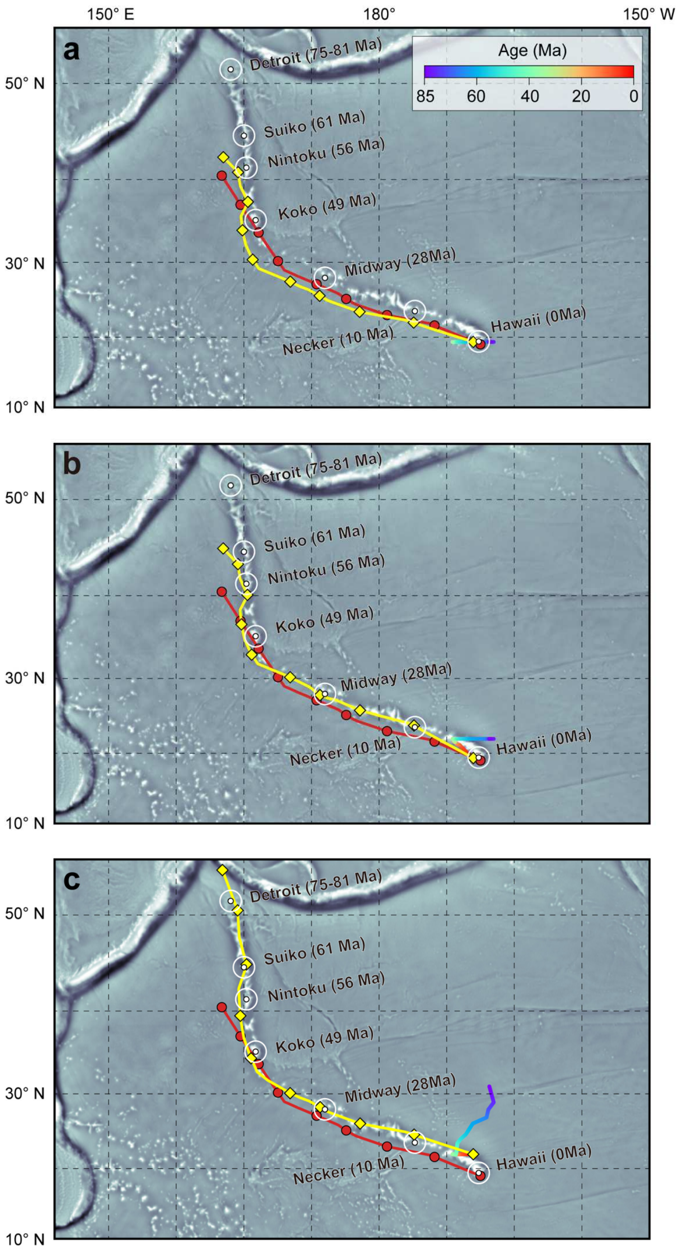

Extended Data Fig. 8. Testing the effect of southward hotspot motion on the HEB angle. Computed hotspot tracks assuming without southward hotspot motion from 80 Ma to the present (**a**), without southward hotspot motion before 47 Ma (**b**), or without hotspot motion after 47 Ma (**c**). Other symbols and legends are the same as Extended Data Fig. 3.

Extended Data Table 1. Reference model parameters.

Parameter	Symbol	Value	Units
Rayleigh number	Ra	6.98×10^{8}	-
Earth radius	R_0	6371	km
Reference density	ρ_0	3930	kg m^{-3}
Thermal diffusivity	κ_0	1×10^{-6}	$m^2\ s^{-1}$
Heat capacity	C_p	1200	J kg^{-1} K^{-1}
Gravitational acceleration	g_0	9.81	m s^{-2}
Thermal expansivity	α_0	3×10^{-5}	K^{-1}
Reference viscosity	η_0	1.0×10^{21}	Pa s
Internal heating	H	59.72	TW
Dissipation number	Di	1.1	-

Extended Data Table 2. Boundary conditions and parameters for mantle flow models

Model	Tcetonic reconstruction	a_0 (Myr ago)	B_{chem}	B_{elco}	A_{slab}	Viscosity profile
M16	M16	230	0.3	0.3	2.8	p1
Hu22	Hu22	230	0.3	0.3	2.8	p1
M19	M19	250	0.3	0.3	2.8	p1
Model 1	C20	250	0.3	0.3	2.8	p1
Model 2	C20	250	0.3	0.5	2.8	p1
Model 3	C20	250	0.3	0.1	2.8	p1
Model 4	C20	250	0.3	0.3	2.8	p2
Model 5	C20	250	0.3	0.3	2.8	p3
Model 6	C20	250	0.3	0.3	5	p1
Model 7	C20	250	0.3	0.3	10	p1
Model 8	C20	250	0.5	0.3	2.8	p1
Model 9	C20	250	0.5	0.3	2	p1
Model 10	C20	250	0.5	0.5	2.8	p1
Model 11	C20	250	0.5	0.7	2.8	p1
M16_Adj	M16	230	0.6	1.091	15	p3
Hu22_Adj	Hu22	230	0.6	1.091	15	p3

M16 and M16_Adj take the plate reconstruction of Müller et al. (2016)[16]; M19 takes the plate reconstruction of Müller et al. (2019)[16]; while for Hu22 and Hu22_Adj, the plate reconstruction of Hu et al. (2022)[11] is used. The models 1-9 uses the Müller et al. (2016)[16] model from 250 Ma to 170 Ma and the revised Clennett et al. (2020)[18] model from 170 Ma to 0 Ma. a_0 is the model start age, B_{eclo} is the buoyancy ratio for eclogite, B_{chem} is the buoyancy ratio for chemical piles, A_{slab} is the dimensionless activation energy for slab.